Distribution Category: Atomic,
Molecular, and Chemical Physics
(UC-411)

ANL/APS/TB--3

DE93 008830

ARGONNE NATIONAL LABORATORY
9700 South Cass Avenue
Argonne, Illinois 60439

ANL/APS/TB-3

Undulator A
Characteristics and Specifications

by B. Lai, A. Khounsary, R. Savoy, L. Moog, and E. Gluskin

Experimental Facilities Division
Advanced Photon Source

February 1993

work sponsored by
U.S. DEPARTMENT OF ENERGY
Office of Energy Research

Undulator A Characteristics and Specifications

B. Lai, A. Khounsary, R. Savoy, L. Moog, and E. Gluskin

Introduction

The Advanced Photon Source (APS) Undulator A is a planar device optimized for the hard x-ray region. In the mature phase of operation, it satisfies the requirement of providing high brilliance x-rays continuously over the tuning range from 4.2 keV to above 30 keV, using the first and the third harmonic radiation from the undulator. This is achieved through the choice of the 3.3-cm long period, the hybrid undulator design, and the stringent requirements on the magnetic field quality. The undulator is 2.4 m long (including the end sections) with 72 periods. The magnetic structure consists of Nd-Fe-B magnets with vanadium permendur poles. Table 1 listed the technical specifications and the parameters for Undulator A. The field errors were specified to ensure that the third harmonic radiation from the actual device will achieve at least 70% of its theoretical brilliance. The first harmonic is less sensitive to field errors and thus should attain brilliance even closer to the theoretical value.

In Table 2, the predicted magnetic fields at various gap values based on a detail design of the magnetic structure of Undulator A are listed. The initial vacuum chamber will provide a minimum gap of 1.55 cm, resulting in first harmonic x-rays from 7 to 14 keV. During mature phase operation, the minimum gap will be reduced to 1.15 cm. This produces a vertical field of 0.70 Tesla at the mid-plane, thus extending the first harmonic range down to 4.2 keV. Fig. 1 shows the first harmonic energy and the deflection parameter K as a function of the gap. Because the magnetic field consists of the fundamental and higher harmonics, the field at mid-plane can be described as

$$B(z) = B_1 \cos(kz) + B_3 \cos(3kz) + \cdots \quad (1)$$

where $k=2\pi/\lambda_u$, λ_u is the period length, and z is measured along the undulator axis. This leads to a peak field of

$$B_{peak} = B_1 + B_3 + \cdots, \quad (2)$$

which is important for power calculations. For spectral analysis, the particle beam instead "sees" an effective field of

$$B_{eff} = \sqrt{B_1^2 + \left(\frac{B_3}{3}\right)^2 + \cdots}. \quad (3)$$

Thus the deflection parameter is defined in terms of the effective field

$$K = 0.934\lambda_u[cm]B_{eff}[Tesla], \quad (4)$$

and the n^{th} harmonic energy is given, in the zero emittance case, by

$$E_n[keV] = \frac{0.95E^2[GeV]n}{\lambda_u[cm]\left(1 + K^2/2 + \gamma^2\theta^2\right)}, \quad (5)$$

where E is the positron beam energy, γ = 1957xE[GeV], and θ is the polar observation angle measured from the undulator axis. Although B_3 increases faster than B_1 as the gap is reduced, the second term in Eq. 3 still contributes less than 1% to the effective field at a minimum gap of 1.15 cm in the case of Undulator A. Thus it is necessary to consider the B_3 term only for power calculations where the peak field is concerned; for spectral calculations, it is sufficient to assume an ideal cosine field of the form $B_1\cos(kz)$.

Positron Source

Radiation characteristics of an undulator depend sensitively on the particle beam parameters. At the APS, the positron beam emittance in the horizontal and the vertical directions are, respectively,

$\varepsilon_x = 8.2\text{x}10^{-9}$ m-rad $\qquad$ $\varepsilon_y = 8.2\text{x}10^{-10}$ m-rad.

The β-functions of the positrons are symmetric about the mid-point of the straight section and have the following values at the center of the undulator

$\beta_x = 14.27$ m $\qquad$ $\beta_y = 10.16$ m.

This results in positron beam sizes of

$\sigma_x = 342$ μm $\qquad$ $\sigma_y = 91$ μm,

and positron beam divergences of

$\sigma_{x'} = 24.1$ μrad $\qquad$ $\sigma_{y'} = 9.1$ μrad.

Due to diffraction effects, the x-ray photons have a source size σ_r and source divergence $\sigma_{r'}$ given by

$$\sigma_r = \sqrt{\lambda L} / 4\pi \qquad \sigma_{r'} = \sqrt{\lambda / L}, \qquad (6)$$

where λ is the wavelength of the x-ray and L is the undulator device length. As a consequence, the phase space of an undulator source is characterized by

$$\Sigma_{x,y} = \sqrt{\sigma_{x,y}^2 + \sigma_r^2} \qquad \Sigma_{x',y'} = \sqrt{\sigma_{x',y'}^2 + \sigma_{r'}^2}. \qquad (7)$$

The dependence on the photon energy for an 2.4 m long undulator at APS is shown in Fig. 2. The source sizes are always dominated by the positron beam, while the divergences are diffraction-limited at low energies. For instance, when Undulator A is at closed gap (4.2 keV), the horizontal and vertical divergences will increase to 26.5 μrad and 14.3 μrad respectively. These numbers are summarized in Table 3. $\Sigma_{x'}$ and $\Sigma_{y'}$ define the central cone of radiation at a particular harmonic and are very useful numbers for the design of beamlines and experiments. In all of the results presented here, both the emittance and the diffraction effects are included. A beam energy of 7 GeV and a stored current of 100 mA are also assumed.

Spectral Brilliance

Spectral brilliance is an important figure of merit used to characterize an undulator source. It is defined as the photon intensity emitted per unit phase space volume of the source, which is an invariant quantity. Fig. 3 shows the expected brilliance at the minimum gap (K=2.17) when observed along the undulator axis (θ=0), and Fig. 4 shows the brilliance at the initial phase (K=1.48). Note the presence of the even and higher harmonics, and that the third harmonic peak decreases relative to the first harmonic peak as K reduces. The first harmonic has a peak brilliance of 2×10^{18}, while that of the third harmonic is also in the 10^{18} range. Because of the low emittance, the brilliance of the second harmonic on-axis is only about 15% of the first harmonic.

As the gap is opened, the positron excursion caused by the undulator field becomes smaller and, therefore, the harmonics shift to shorter wavelengths according to Eq. 5. Fig. 5 and 6 follow the first and the third harmonic spectra as the gap is widened and the value of K is reduced. The brilliance of the first harmonic decreases slowly, while that of the third harmonic decays at a faster rate. As K gets smaller, the higher harmonics contribute less to the overall spectrum. At the same time, the energy width of

the harmonics increases. The shape of the harmonics is always asymmetric, with the emittance effect broadening mainly the low energy side of the peak. Despite the asymmetry, the FWHM is still a useful quantity for characterizing the energy bandwidth $\Delta E/E$. Interestingly enough, the energy bandwidth defined in this way has almost a linear relation to the peak energy of the harmonic, which is indicated in Fig. 7. It is well known that the third harmonic has a narrower $\Delta E/E$ than the first harmonic. Thus at the closed gap of 1.15 cm, the first harmonic has an energy width of $\Delta E = 0.1$ keV ($E_1 = 4.2$ keV) while the third harmonic has a width of 0.14 keV ($E_3 = 12.6$ keV). When the gap is nearly open, ΔE will increase to about 0.6 keV for the first harmonic at an energy of $E_1 =$ 13 keV and about 0.8 keV for the third harmonic at $E_3 = 40$ keV.

By tracing the peak brilliance as the gap changes, one can obtain a tuning curve like the one shown in Fig. 8 for Undulator A. It indicates continuous coverage from 4.2 to higher than 30 keV with the brilliance changes no more than an order of magnitude. The brilliance for the first harmonic is actually fairly constant, with variation within a factor of two in most cases. Note the second harmonic can be used during the initial phase to bridge the tuning range of the first and the third harmonics. This is even more favorable when one considers that the second harmonic has more of its photons emitted off-axis and that most beamlines do have finite acceptance. This will be discussed in more detail in the following two sections.

Angular Distribution

The on-axis brilliance presented in the last section is measured at one point in phase space at the source, namely $x=y=x'=y'=0$. The photon intensity actually has a rather complex distribution in phase space. At a particular harmonic energy E_n, most of the x-rays are inside the central cone, which is nearly Gaussian in shape with the Σs defined in Eq. 7. As the observation angle moves further off-axis, one encounters radiation red-shifted from the n+1, n+2 harmonics and so on. This is uniquely described by Eq. 5 in the zero-emittance case. Finite emittance smears out the well-defined angular structure from Eq. 5. In the case of APS emittance, Figs. 9-11 show a simulation of the angular distribution of the photons at the first, second, and third harmonic energies. The central cone of radiation is well separated from the higher harmonics in all cases. Due to the lower energy, the central cone for the first harmonic (Fig. 9) is noticeably larger than that for the third harmonic (Fig. 10), especially in the vertical direction, as predicted by Eq. 6. In both cases, a beamline acceptance on the order of 0.14 x 0.07 mrad^2 will be able to extract the entire central cone, which contains about 67% of the total flux

available at E_1 and about 50% at E_3. For smaller K values, this ratio increases because the higher harmonics become relatively weaker. Outside of the central cone, all the off-axis harmonic contributions merge into a band of radiation. At the first harmonic, this band extends to about θ=0.15 mrad. For the third harmonic, the off-axis radiation appears at smaller angles, as expected from Eq. 5, but is still distinguishable from the central cone. The implication is that more photons can be collected if the beamline can accept the off-axis harmonic radiation outside of the central cone, but there will essentially be no intensity gain beyond an acceptance of 0.3 x 0.3 mrad^2.

Angular distribution of the second harmonic (Fig. 11) is slightly different from that of the first and the third harmonics. At the "true" second harmonic energy of E_2=8.4 keV (E_1=4.2 keV), there is few photons on-axis. However, there is actually more photons near the center at a lower energy of 8.2 keV. This can also be seen from the on-axis brilliance spectrum in Fig. 3, where the peak of the second harmonic is located at 8.2 keV. The angular distribution of these photons resembles, but is actually broader than, the central cones of the first and the third harmonics. The reason is in the zero-emittance case the maximum intensity for the second harmonic is located off-axis at an energy below E_2. Finite beam emittances serve to distribute some of these photons back on-axis.

Spectral Flux through an Aperture

Spectral brilliance like that shown in Fig. 3 is obtained only at one observation point. At the other extreme is the spectrum of the total photon flux integrated over all angles as shown in Fig. 12. The peaks are clearly broader, especially at the low energy side of each harmonic, and the general background is higher. Also note in the initial phase (K=1.48) the photon flux ratio of the second harmonic to the first harmonic is more than 50%, while it is only 15% in the case of brilliance (Fig. 4). These changes are a consequence of the angular distribution discussed in the last section. In a usual beamline, the actual spectrum observed will be somewhere between these two extreme cases due to the finite acceptance. The use of an aperture also serves the purpose of limiting the power loading on the optics. Figs. 13-15 show the photon flux spectra of the first three harmonics, through apertures of various size for the mature phase. Because a larger percentage of the photons are located outside of the central cone for the third harmonic, a smaller aperture will affect the spectral flux available to the higher harmonics more than that to the first harmonic. The use of an aperture also affects the sharpness of the harmonics. For instance at closed gap (K=2.17), with a 100 x 100 μrad^2 aperture, the FWHM of the first harmonic is increased to 0.47 keV and the third harmonic to 0.40 keV.

Figs. 16-18 show similar photon flux spectra for the initial phase (K=1.48). Note that with an acceptance of 100 x 100 μrad^2, the second harmonic can provide spectral flux up to 2.5×10^{14} ph/s/0.1% compared to 6.7×10^{14} from the first harmonic.

Tapering

In addition to using an aperture, the spectrum of a harmonic can be further broadened by tapering the undulator. Undulator A offers the capability of tapering the magnetic gap up to 4 mm between the two ends of the undulator at any gap setting. Because the value of K is changing throughout the undulator, a range of harmonic energy is obtained according to Eq. 5 and, hence, the broadening. To the first approximation, the bandwidth increase due to tapering can be estimated by

$$\frac{\Delta E}{E_{av}} \approx \left(\frac{K_{av}^2}{1 + K_{av}^2 / 2} \right) \frac{\pi \Delta G}{\lambda_u}, \qquad (8)$$

where ΔG is the amount of gap tapering, K_{av} is the average K in the undulator, and E_{av} is the energy corresponding to the deflection parameter K_{av}. This should be convoluted with the bandwidth in the untapered case in order to obtain the total bandwidth when the undulator is tapered. Eq. 8 indicates that the bandwidth increase $\Delta E/E$ is mostly linear with the tapering amount and that tapering has the biggest effect near closed gap when K is large. Fig. 19 illustrates the energy width ΔE produced by a 1-mm taper when the overall gap is tuned to various average energies of the first harmonic. It shows that an energy width of 0.4-0.6 keV can be obtained throughout most of the tuning range of the first harmonic using a 1-mm taper. For larger gap tapering, Eq. 8 indicates that the energy width is simply proportional to ΔG.

Another interesting point from Eq. 8 is that, for a particular tapering configuration, the energy width ΔE is proportional to the harmonic number n, because $E_{av} \approx E_n$. Therefore, certain higher harmonics may be broadened enough that they will merge into one another and produce a continuous spectrum, while the lower harmonics still remain separate. This is shown in Fig. 20 for the cases of no tapering and maximum tapering near the closed gap. The first harmonic has been broadened into an energy band of about 2.3 keV width, and the second and the third harmonics are no longer distinguishable. This suggests that in order to obtain a broader spectrum at a particular energy, one can taper the undulator either with the first harmonic tuned to that range, or by closing the gap more and using the higher harmonics. Each has different implications

on the power loading and the spectrum one can obtain. Using Eq. 8, the width of the first harmonic can be estimated to be ΔE=2.6 keV (E_{av}=5.6 keV, K_{av}=1.74). Although for this 4-mm tapering case, the brilliance has been reduced to the 1-2 x10^{17} range, this is still substantially higher than the brilliance one can generally obtain from a wiggler of similar critical energy at the APS. Fig. 21 shows in more detail some of the intermediate cases for the first harmonic. It is obvious that through tapering one can continuously trade brilliance for larger ΔE (up to the ΔE_{max} set by the 4-mm limit). The parameters for the three tapering cases are summarized in Table 4. Note that the energy widths ΔE calculated using Eq. 8 are in reasonably agreement with the FWHMs from Fig. 21.

Tapering also affects the angular distribution of the x-rays. This is shown in Fig. 22 along the horizontal and the vertical directions. For 4-mm tapering, the opening angle is on the order of 50 μrad. This is still fairly collimated compared to wiggler radiation, particularly in the horizontal direction. The increase in the opening angle is a direct consequence of Eq. 5 when more than one value of K is present. It indicates that, at the photon energy E_{hv}, the opening angle is approximately given by

$$\theta = \frac{1}{\gamma}\sqrt{\frac{0.95E^2[\mathrm{GeV}]n}{\lambda_u[\mathrm{cm}]E_{hv}[\mathrm{keV}]} - 1 - \frac{K_{min}^2}{2}}, \qquad (9a)$$

where $1/\gamma$=73 μrad for the APS, and K_{min} is the deflection parameter corresponding to the large gap end of the tapered undulator. This predicts θ=53 μrad for 4-mm tapering, which is in reasonable agreement with the simulation. Eq. 9a can be written more simply as

$$\theta = \frac{1}{\gamma}\sqrt{\frac{K_{hv}^2 - K_{min}^2}{2}} \qquad (9b)$$

where K_{hv} is the deflection parameter corresponding to the energy of interest E_{hv}. Eq. 9 clearly indicates that the opening angle due to tapering is a function of the energy, and θ becomes larger as one moves toward the low energy side of the energy band.

Thermal Load

When the APS is operated at 7 GeV with 100 mA stored current, Undulator A will generate a beam with a total power of about 3.8 kW and a peak power density of about 133 kW/mrad^2 at the closed gap of 1.15 cm. The normal incident heat flux on a component at 30 m from the source is about 148 W/mm^2. Thermal management of the

front end and optical components subjected to the high heat flux synchrotron beam is a major component design consideration, and therefore some basic power information is given here.

The specifications of Undulator A are already given in Table 1. Figure 23 displays the variation of the beam power with undulator gap. Also shown on the same figure is the beam power that passes through square apertures of various sizes. Of particular interest is the fact that, for example, a 100 μrad x 100 μrad aperture will let through 1.03 kW or 27% of the total beam. The opening size of this aperture, if located at 30 m from the source is 3 mm x 3 mm.

The peak power density of the APS Undulator A beam as a function of the gap opening is shown in Figure 24. The corresponding normal incidence peak heat flux at 30 m from the source is also shown in Figure 24.

Table 1 Undulator A parameters and specifications

Device	**Undulator A**
Undulator Period, λ_u [cm]	3.3
Number of Periods, N	72
Device Length, L [m]	2.4
Minimum Gap (initial phase) [cm]	1.55
Minimum Gap (mature phase) [cm]	1.15
Deflection Parameter, K_{eff} (K_{max}) *	2.17 (2.23)
Maximum Field, B_{eff} (B_{peak}) [T] *	0.70 (0.72)
First Harmonic Energy E_1 [keV] *	4.2
Characteristic Energy, E_c [keV] *	23.5
Random Field Error (rms)	< 0.5%
Phase Error (rms)	< 8 degrees

* Quantities evaluated at minimum gap of 1.15 cm.

Table 2 Predicted values of the field, the deflection parameter, and the first harmonic energy as a function of the gap.

APS Undulator A
(period = 3.3 cm)

Gap [cm]	Peak Field [T]	Eff. Field [T]	K	E_1 [keV]
1.15	**0.722**	**0.703**	**2.17**	**4.21**
1.20	0.687	0.670	2.07	4.50
1.30	0.622	0.609	1.88	5.10
1.40	0.564	0.554	1.71	5.73
1.50	0.511	0.504	1.55	6.39
1.55	**0.487**	**0.481**	**1.48**	**6.72**
1.60	0.464	0.458	1.41	7.06
1.70	0.421	0.417	1.28	7.73
1.80	0.382	0.379	1.17	8.39
1.90	0.347	0.344	1.06	9.02
2.00	0.315	0.313	0.965	9.62
2.50	0.195	0.194	0.600	12.0
3.00	0.121	0.121	0.373	13.2
3.50	0.0751	0.0751	0.231	13.7
4.00	0.0466	0.0466	0.144	14.0

Table 3 Source parameters for Undulator A

Positron Energy, E [GeV]	7
Stored Current [mA]	100
Positron Beam Emittance [m-rad] :	
Horizontal, ε_x	8.2×10^{-9}
Vertical, ε_y	8.2×10^{-10}
Betatron Function [m] :	
Horizontal, β_x	14.27
Vertical, β_y	10.16
Positron Beam Size, standard Deviation [μm] :	
Horizontal, σ_x	342
Vertical, σ_y	91
Positron Beam Divergence, standard Deviation [μrad] :	
Horizontal, $\sigma_{x'}$	24
Vertical, $\sigma_{y'}$	9
Intrinsic Photon Size, standard Deviation σ_r [μm]*	2.1
Intrinsic Photon Divergence, standard Deviation $\sigma_{r'}$ [μrad]*	10.9
Total Photon Source Size, standard Deviation [μm] : *	
Horizontal, Σ_x	342
Vertical, Σ_y	91
Total Photon Source Divergence, standard Deviation [μr] : *	
Horizontal, $\Sigma_{x'}$	26
Vertical, $\Sigma_{y'}$	14

* Quantities evaluated at first harmonic energy of 4.2 keV.

Table 4 Tapering parameters for Fig. 20-22.

APS Undulator A
(period = 3.3 cm)

Tapering [mm]	**0**	**1**	**2**	**4**
Min. Gap [cm]	1.2	1.2	1.2	1.2
Max. Gap [cm]	1.2	1.3	1.4	1.6
K_{max}	2.07	2.07	2.07	2.07
K_{min}	2.07	1.88	1.71	1.41
K_{av}	2.07	2.97	1.89	1.74
E_{av} [keV]	4.5	4.8	5.1	5.6
ΔE_{calc} [keV]	-	0.60	1.2	2.6
ΔE_{simu} [keV]	0.1	0.55	1.1	2.3
θ_{calc} [μrad]	-	30	40	53

ΔE_{calc} : from Eq. 8.

ΔE_{simu} : FWHM from Fig. 20 and 21.

θ_{calc} : from Eq. 9

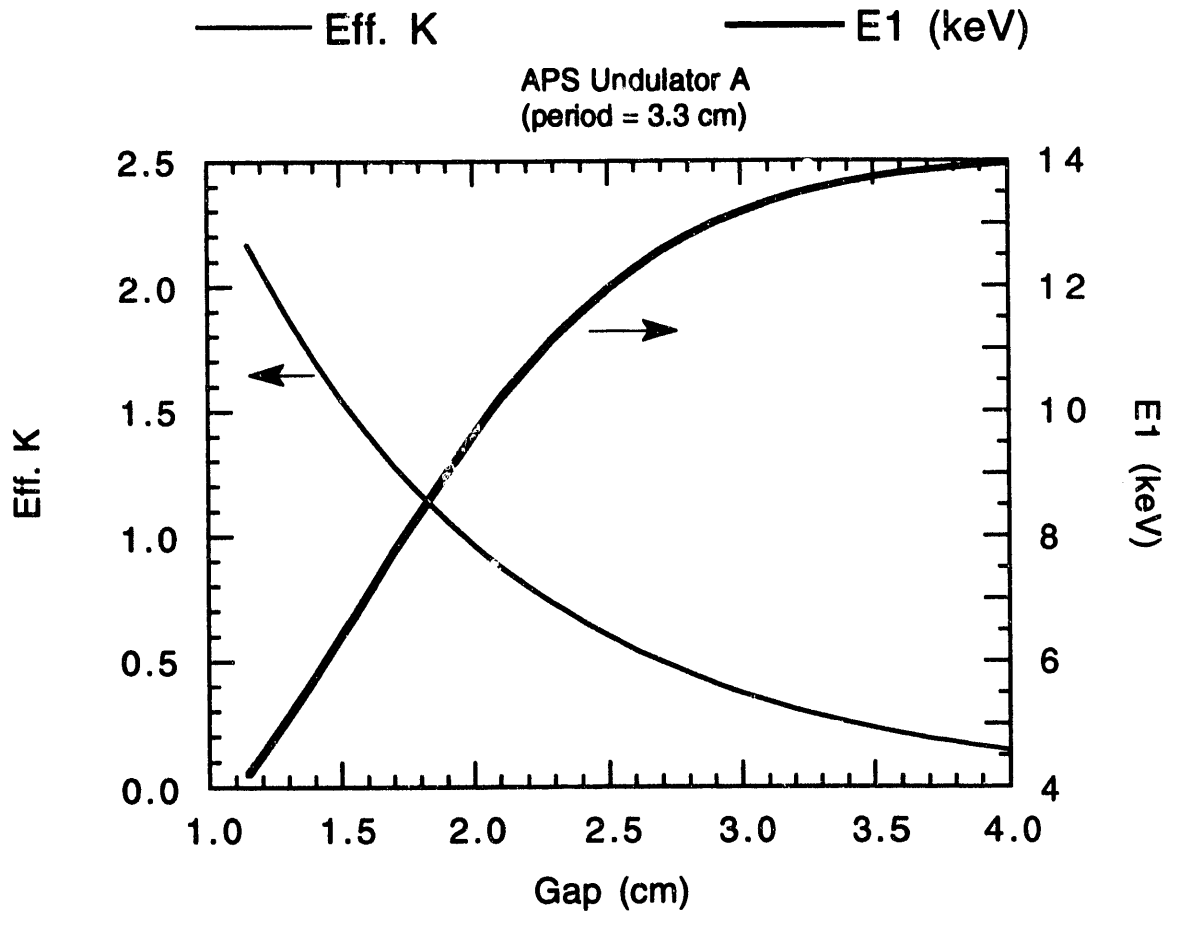

Fig. 1 Deflection parameter and the first harmonic energy as a function of the gap for the Undulator A calculated using the values in Table 2.

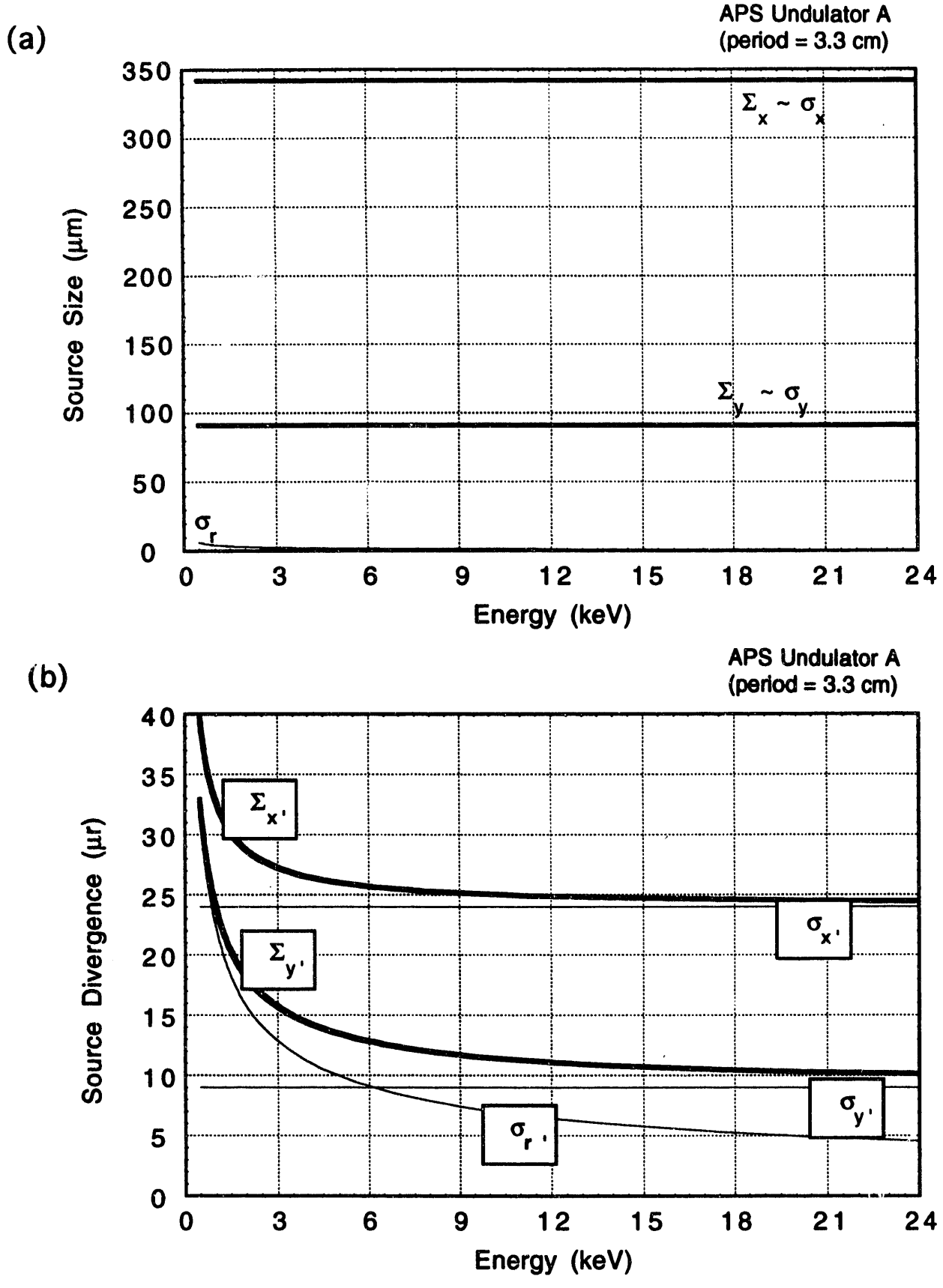

Fig. 2 (a) Radiation source size and (b) source divergence as a function of photon energy from a device with L=2.4 m. These values can also be used for other undulator sources at APS.

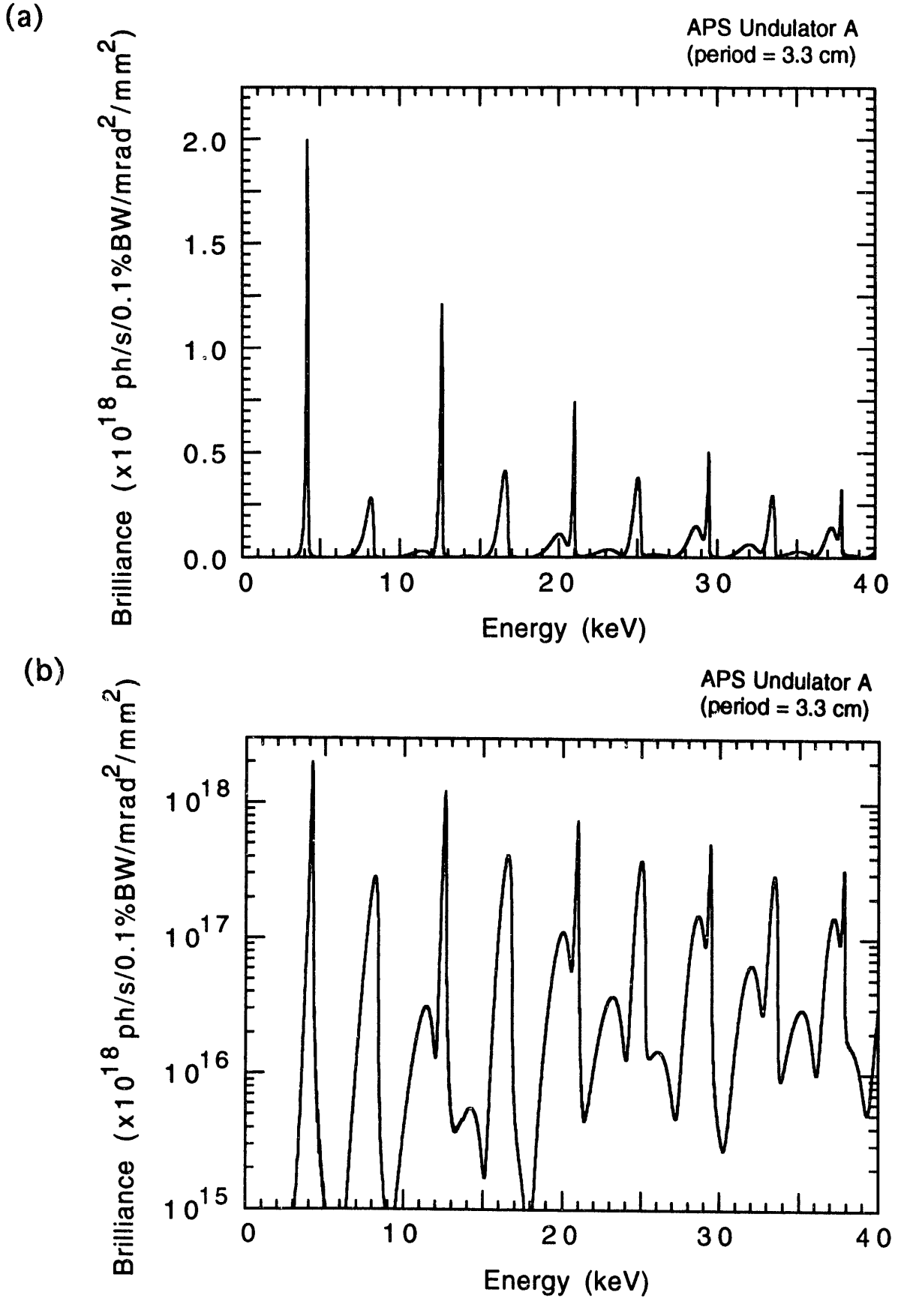

Fig. 3 (a) Linear and (b) logarithmic plot of the on-axis brilliance spectrum for Undulator A at the closed gap of 1.15 cm (K=2.17). Note the presence of even and higher harmonics. (Operation at 7 GeV, 100 mA).

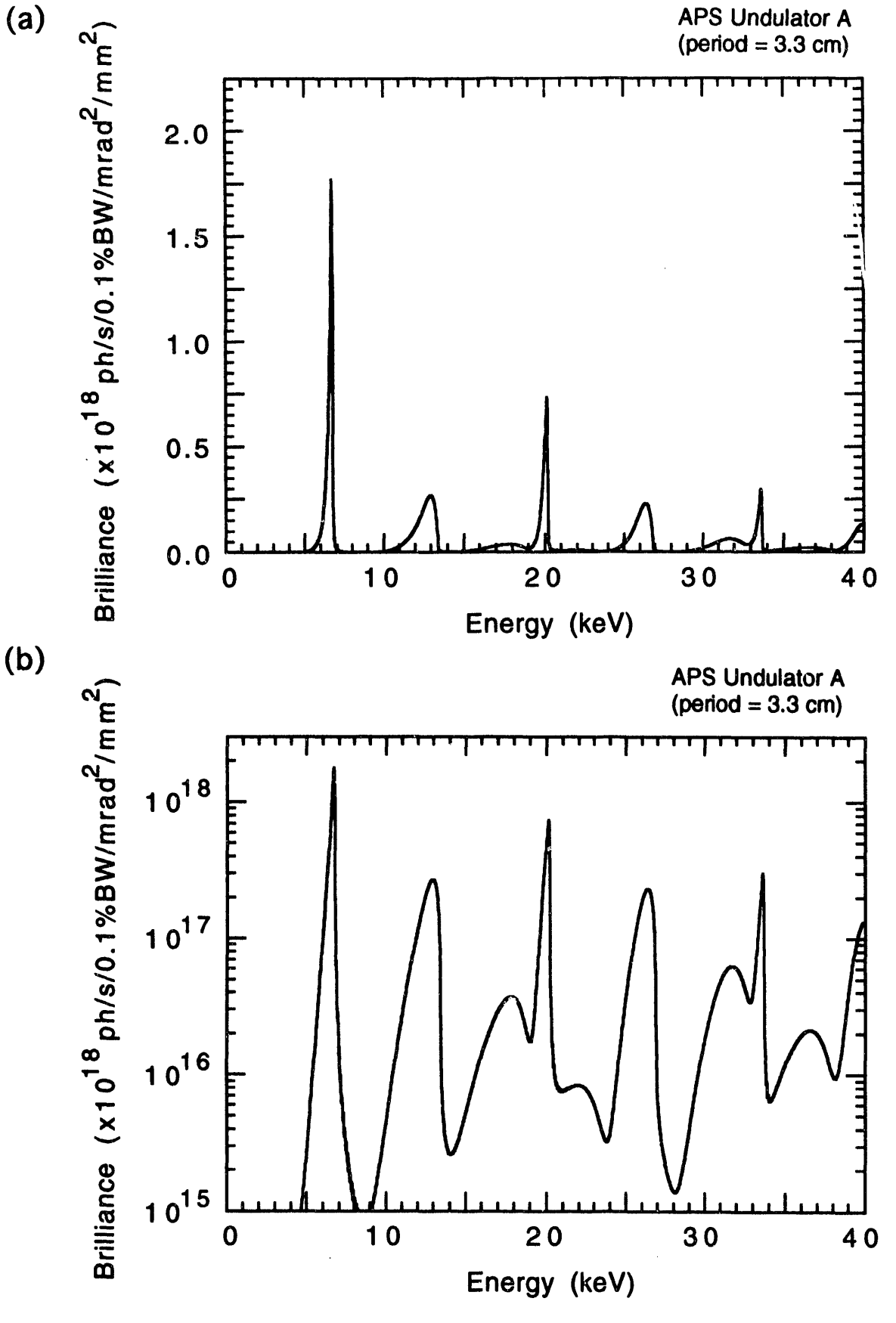

Fig. 4 (a) Linear and (b) logarithmic plot of the on-axis brilliance spectrum for Undulator A at the initial gap of 1.55 cm (K=1.48). Note the presence of even and higher harmonics. (Operation at 7 GeV, 100 mA).

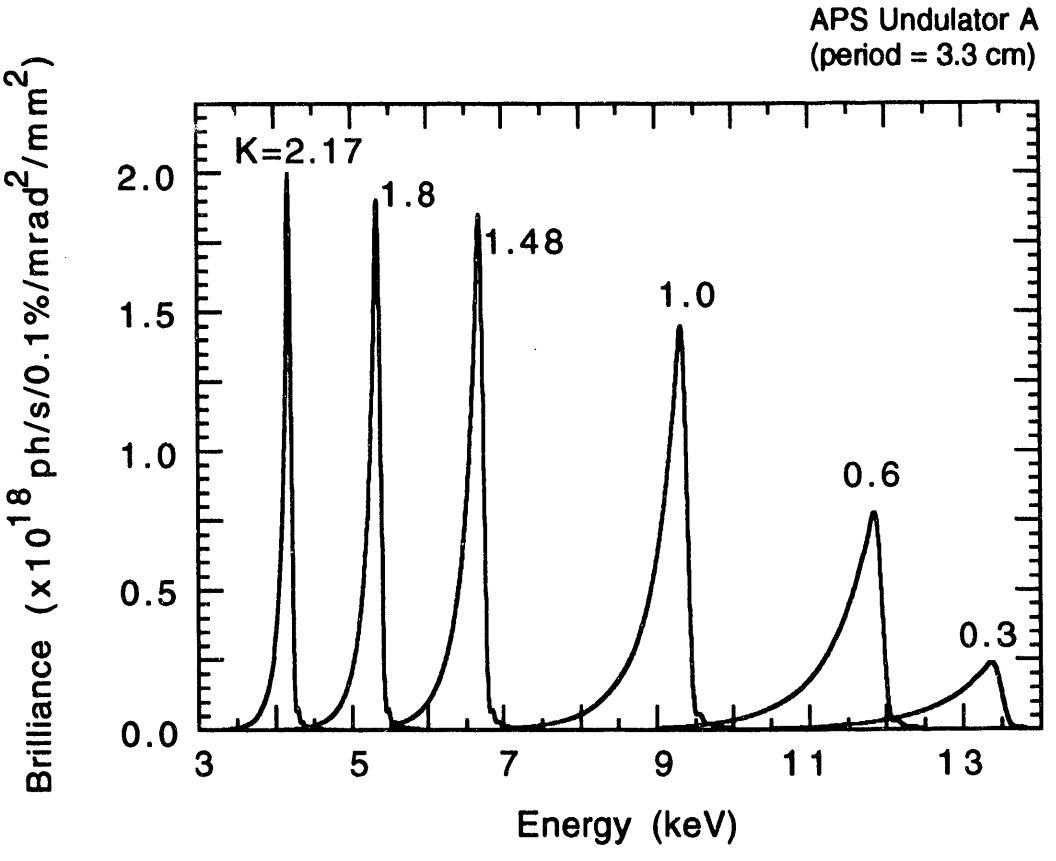

Fig. 5 On-axis brilliance spectra of the first harmonic at different gap settings. Note K=1.48 in the initial phase, and K=2.17 in the mature phase operation. (Operation at 7 GeV, 100 mA).

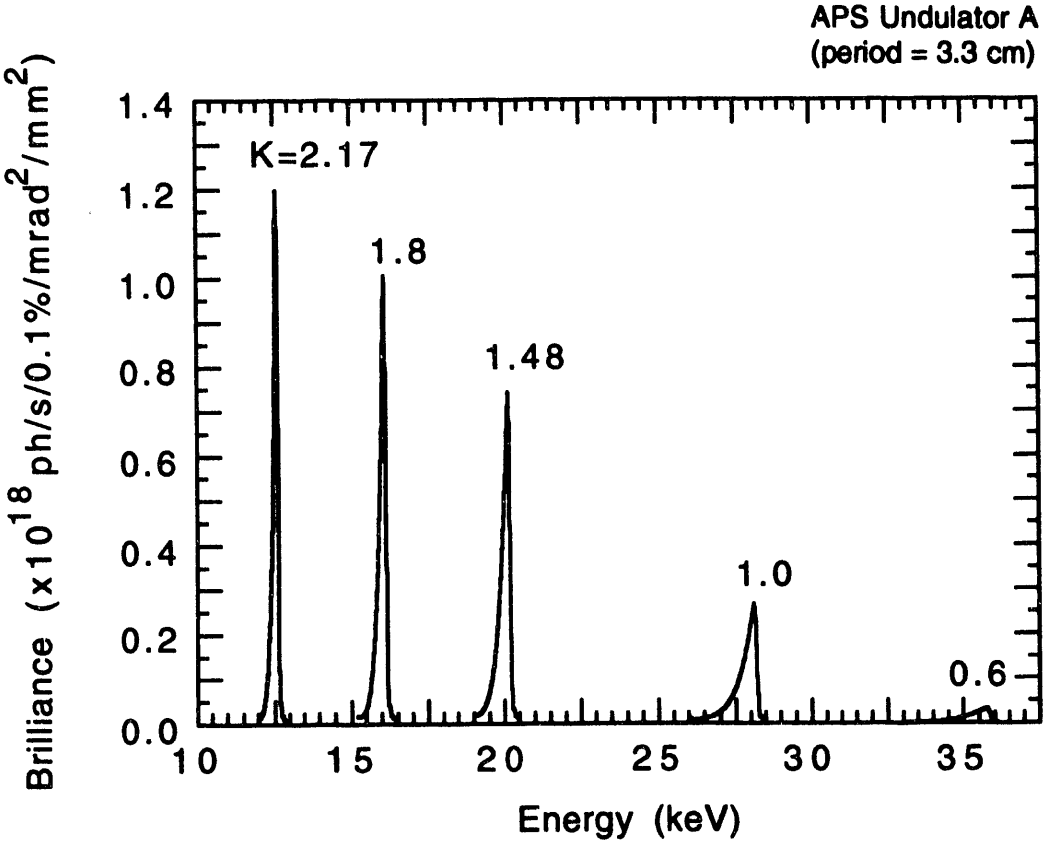

Fig. 6 On-axis brilliance spectra of the third harmonic at different gap settings. Note that as K gets small the peak decreases faster than the first harmonic. (Operation at 7 GeV, 100 mA).

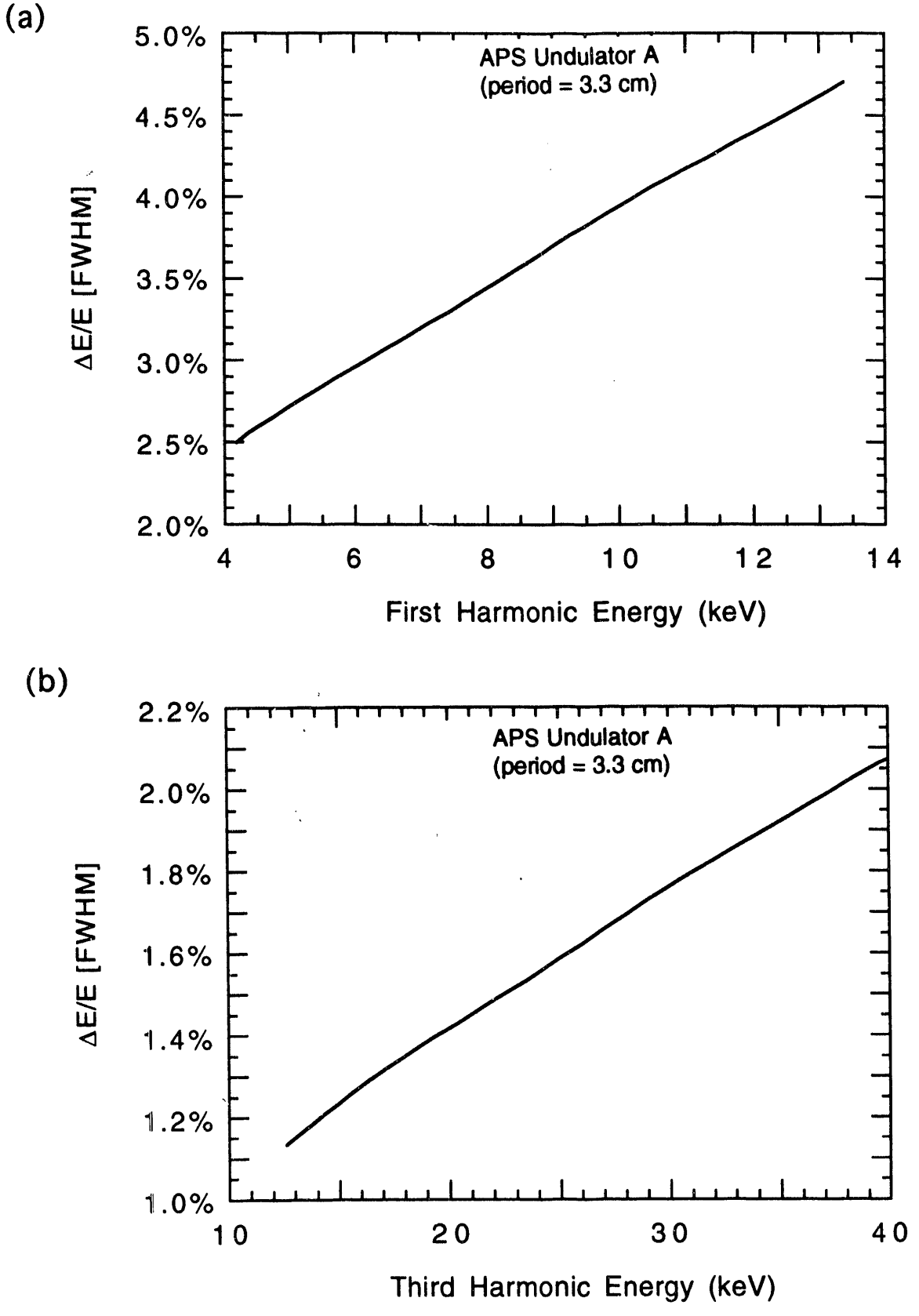

Fig. 7 Bandwidth of (a) the first and (b) the third harmonic measured using the FWHM from Fig. 5 and 6.

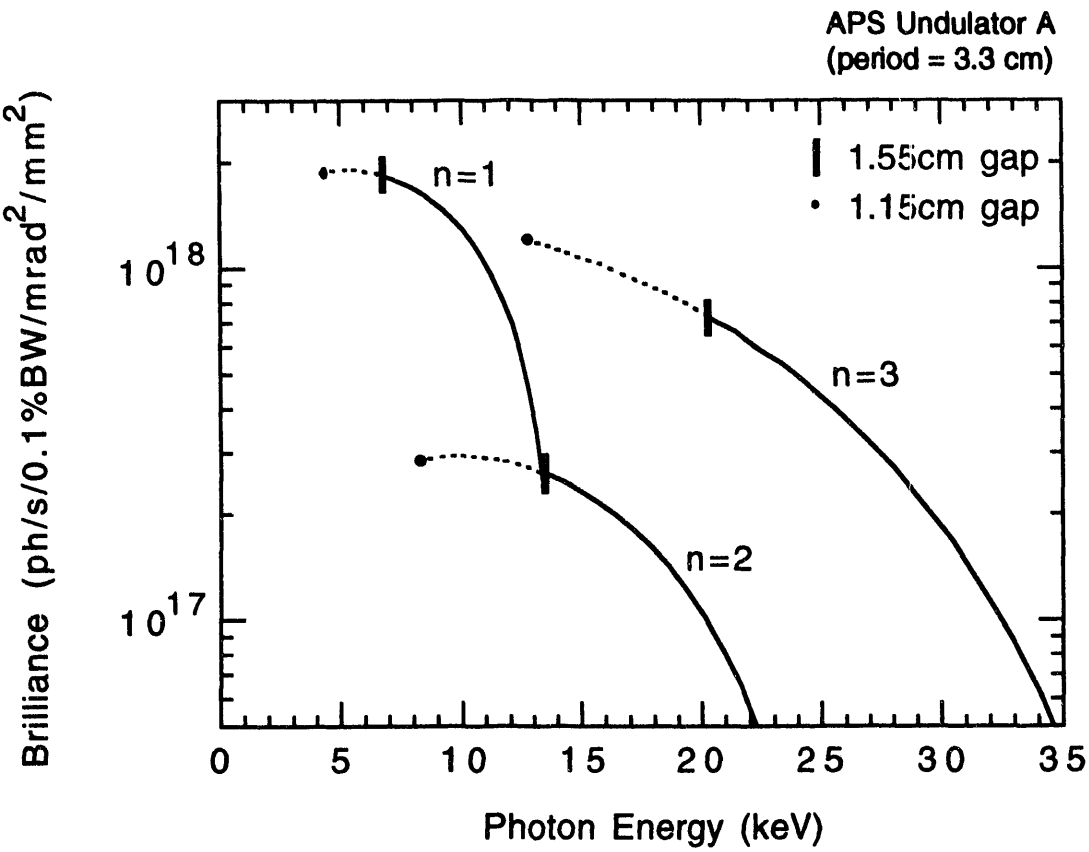

Fig. 8 Tuning curve using the peak on-axis brilliance from the first, second, and third harmonics. The dashed lines indicate mature phase operation. (Operation at 7 GeV, 100 mA).

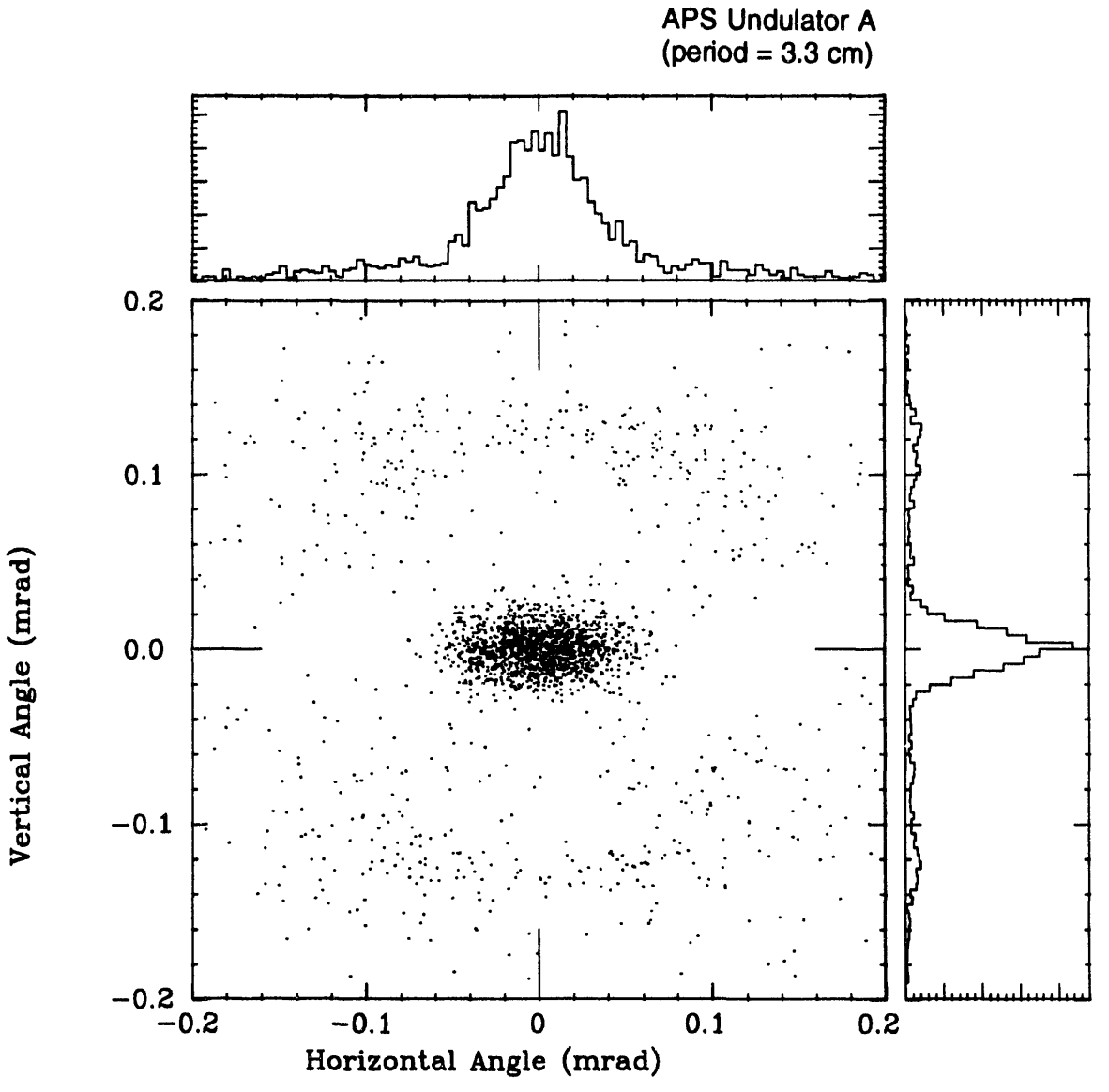

Fig. 9 Monte-Carlo simulation of the angular distribution at the first harmonic energy (E=4.2 keV) at closed gap (K=2.17). The histograms are obtained from integrating along either the horizontal or the vertical direction.

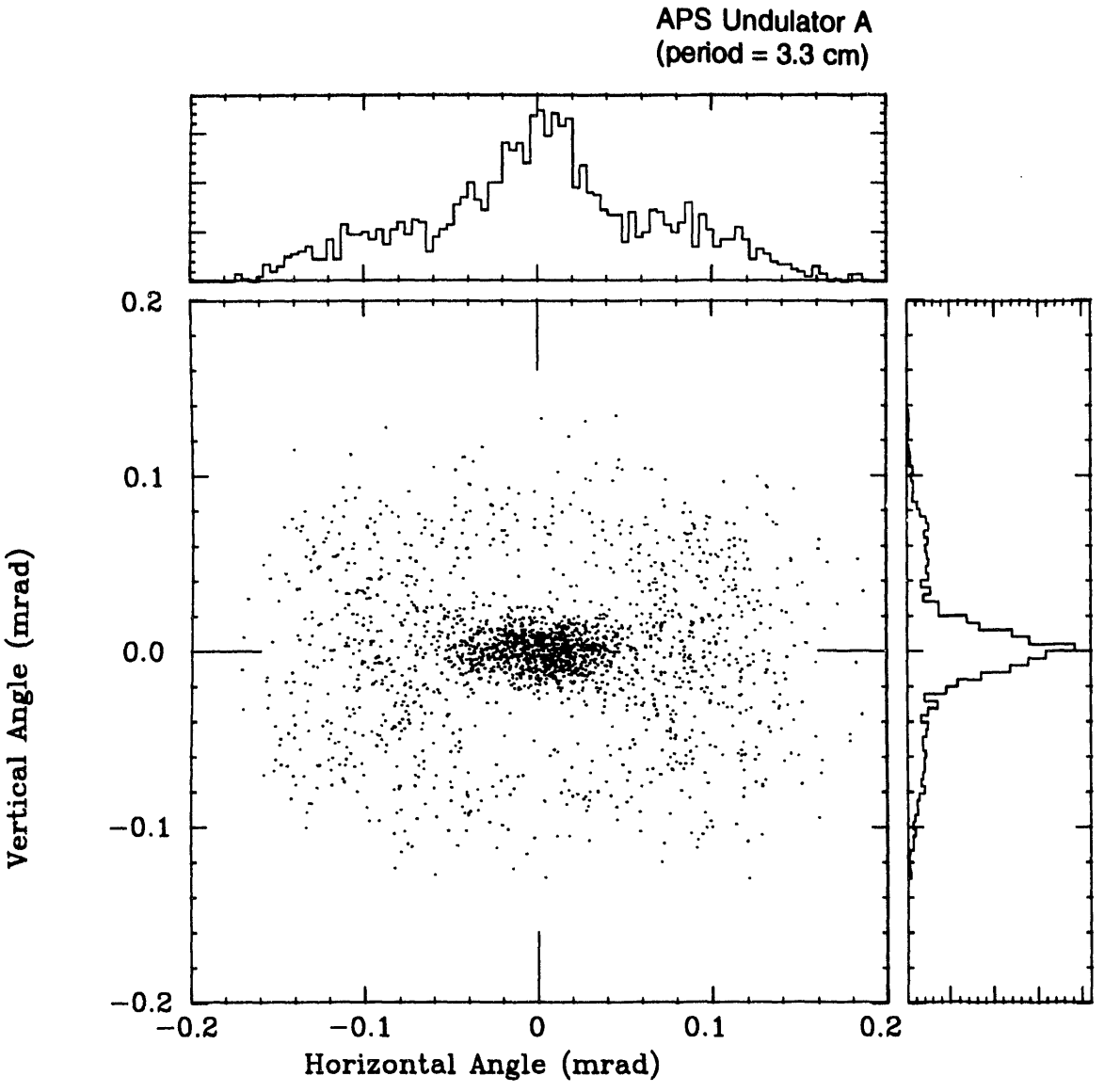

Fig. 10 Monte-Carlo simulation of the angular distribution at the third harmonic energy (E=12.6 keV) at closed gap (K=2.17). The histograms are obtained from integrating along either the horizontal or the vertical direction.

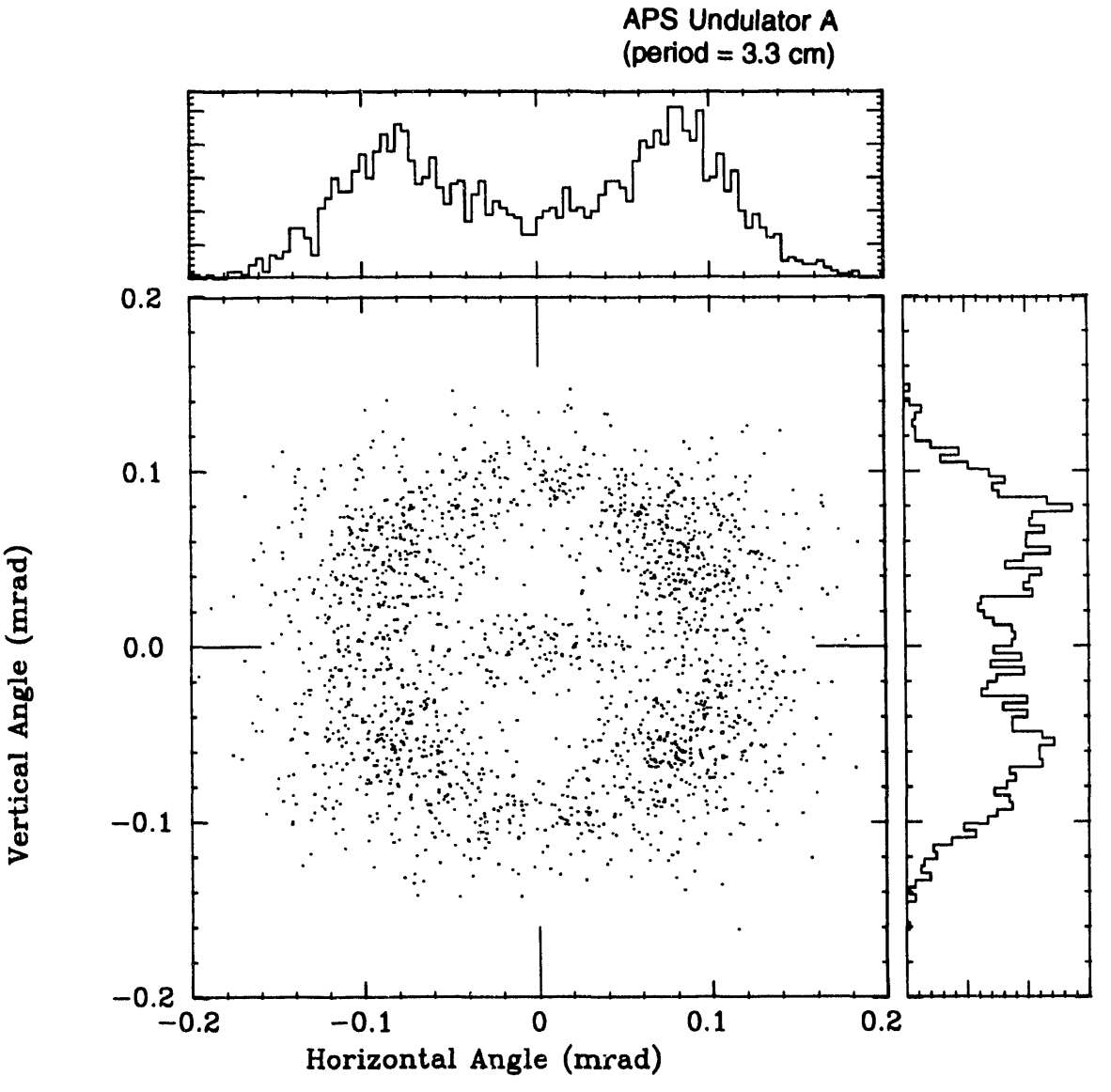

Fig. 11(a) Monte-Carlo simulation of the angular distribution for the second harmonic at 8.4 keV (K=2.17). The histograms are obtained from integrating along either the horizontal or the vertical direction.

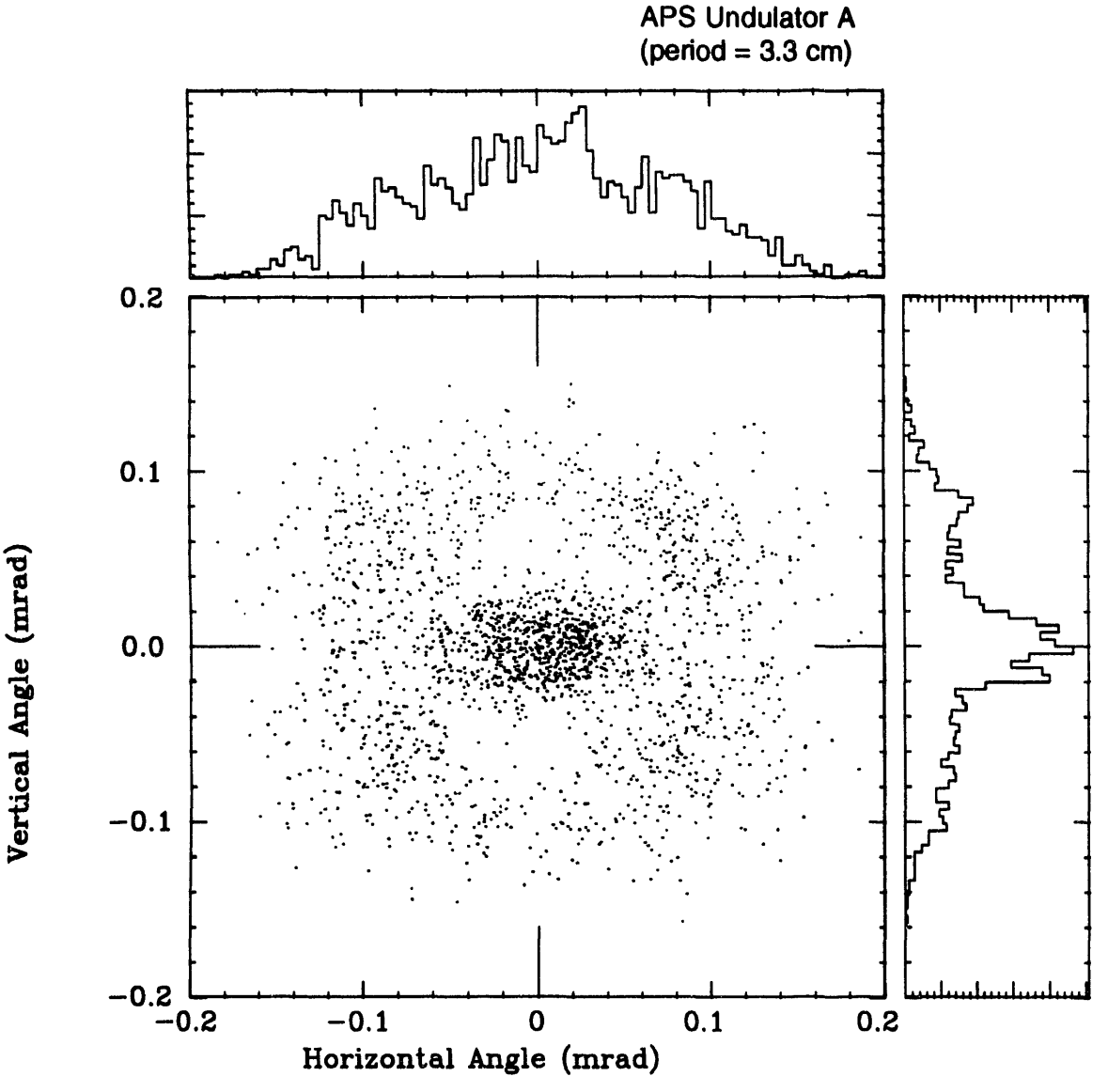

Fig. 11(b) Monte-Carlo simulation of the angular distribution for the second harmonic at 8.2 keV (K=2.17). The histograms are obtained from integrating along either the horizontal or the vertical direction.

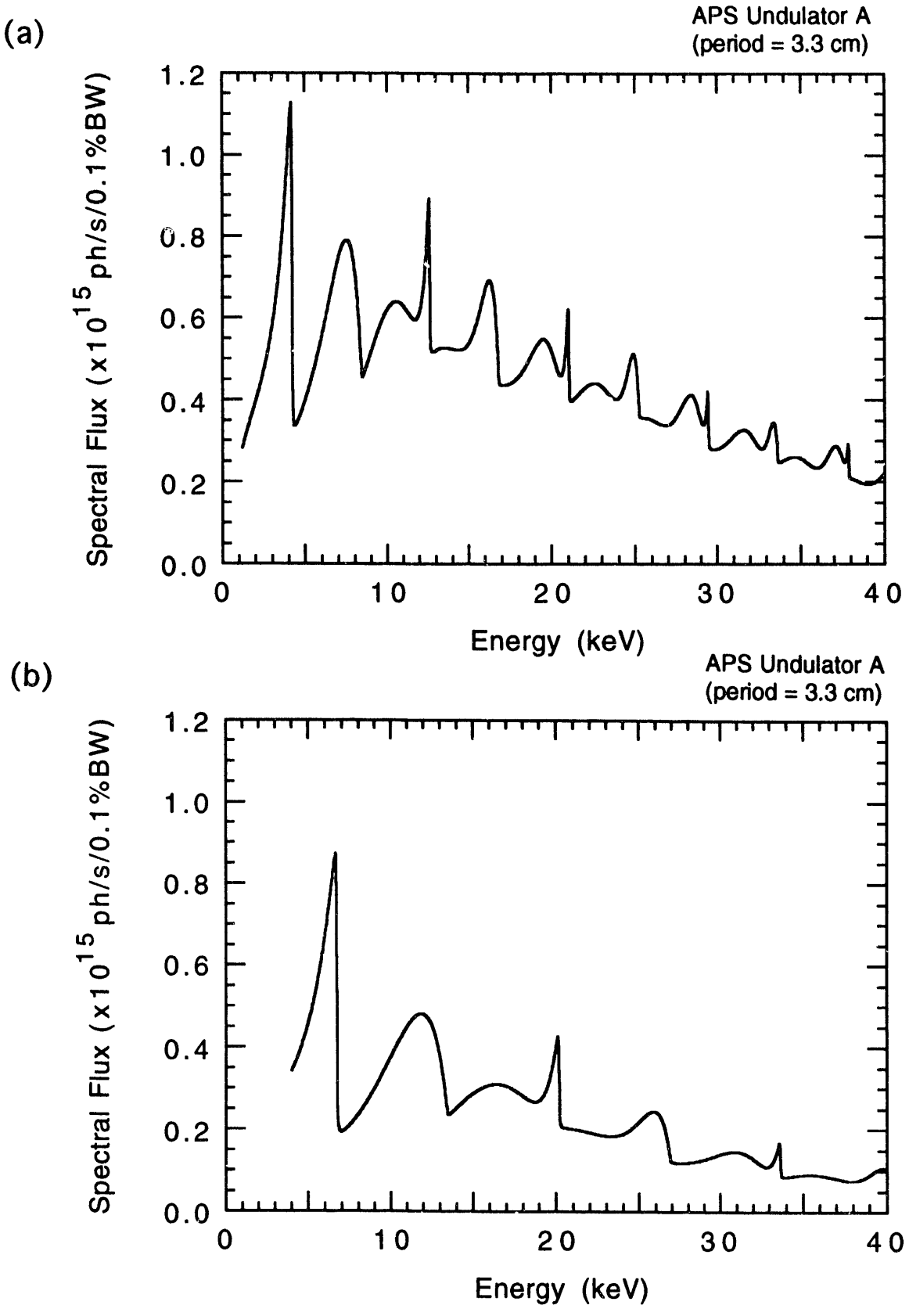

Fig. 12 Spectral flux integrated over all angles at closed gap for (a) the mature phase (K=2.17) and (b) the initial phase (K=1.48). (Operation at 7 GeV, 100 mA).

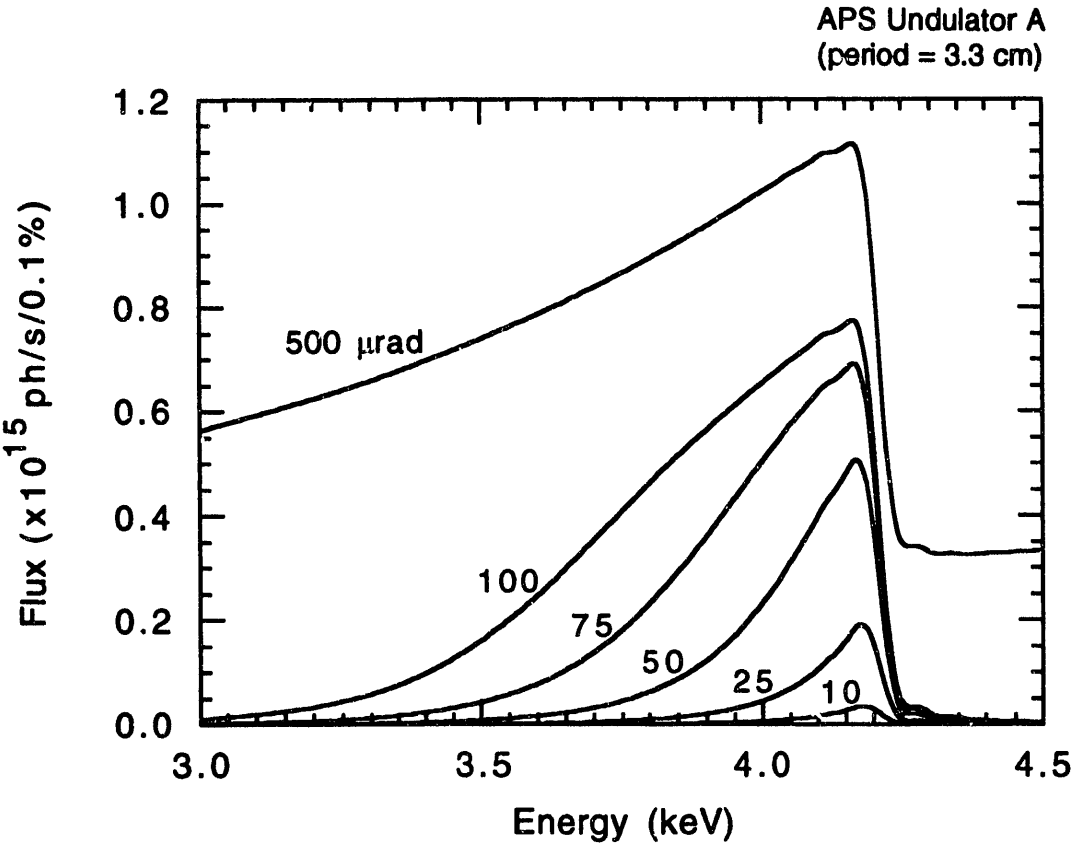

Fig. 13 Spectral flux of the first harmonic through square apertures of various sizes for the mature phase (K=2.17). (Operation at 7 GeV, 100 mA).

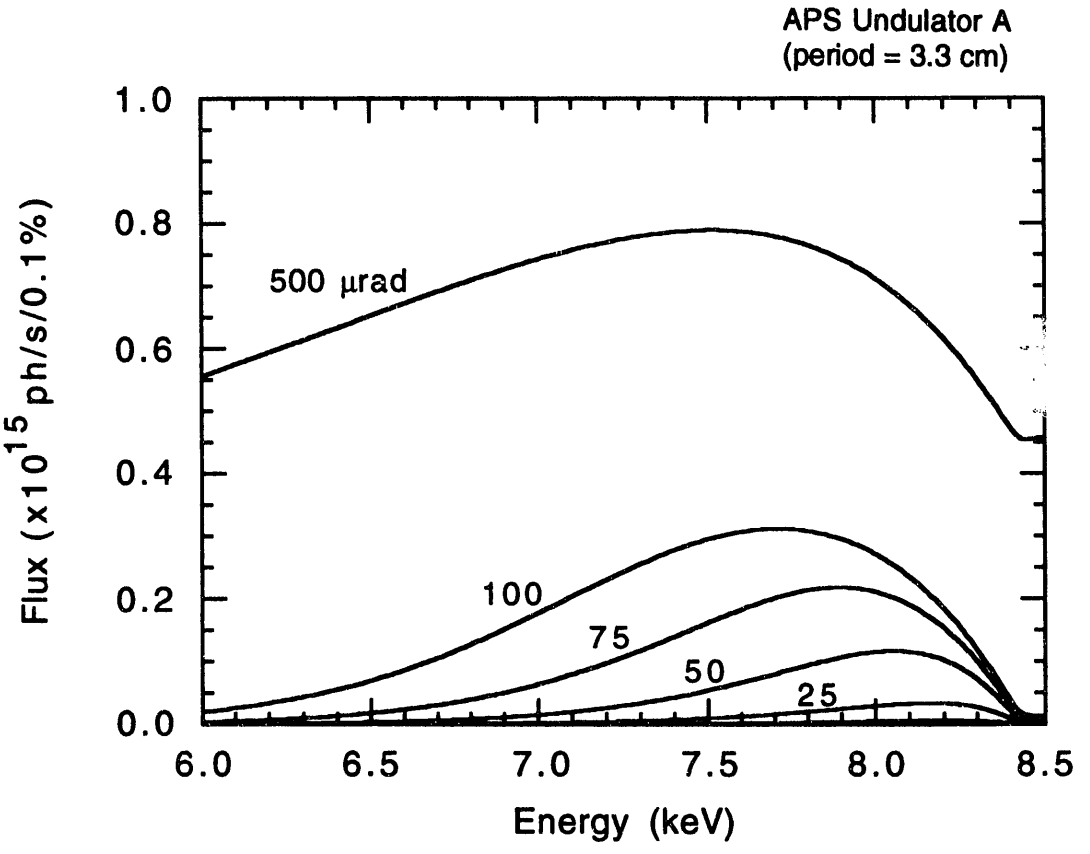

Fig. 14 Spectral flux of the second harmonic through square apertures of various sizes for the mature phase (K=2.17). (Operation at 7 GeV, 100 mA).

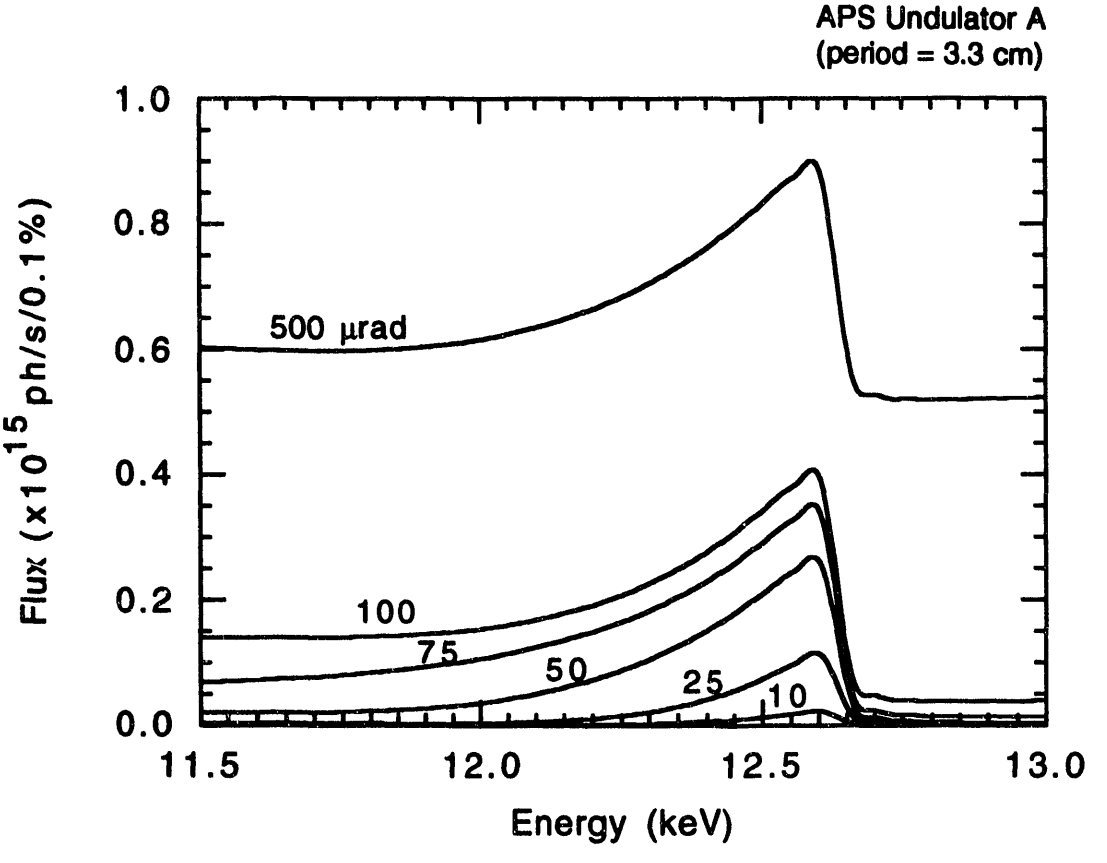

Fig. 15 Spectral flux of the third harmonic through square apertures of various sizes for the mature phase (K=2.17). (Operation at 7 GeV, 100 mA).

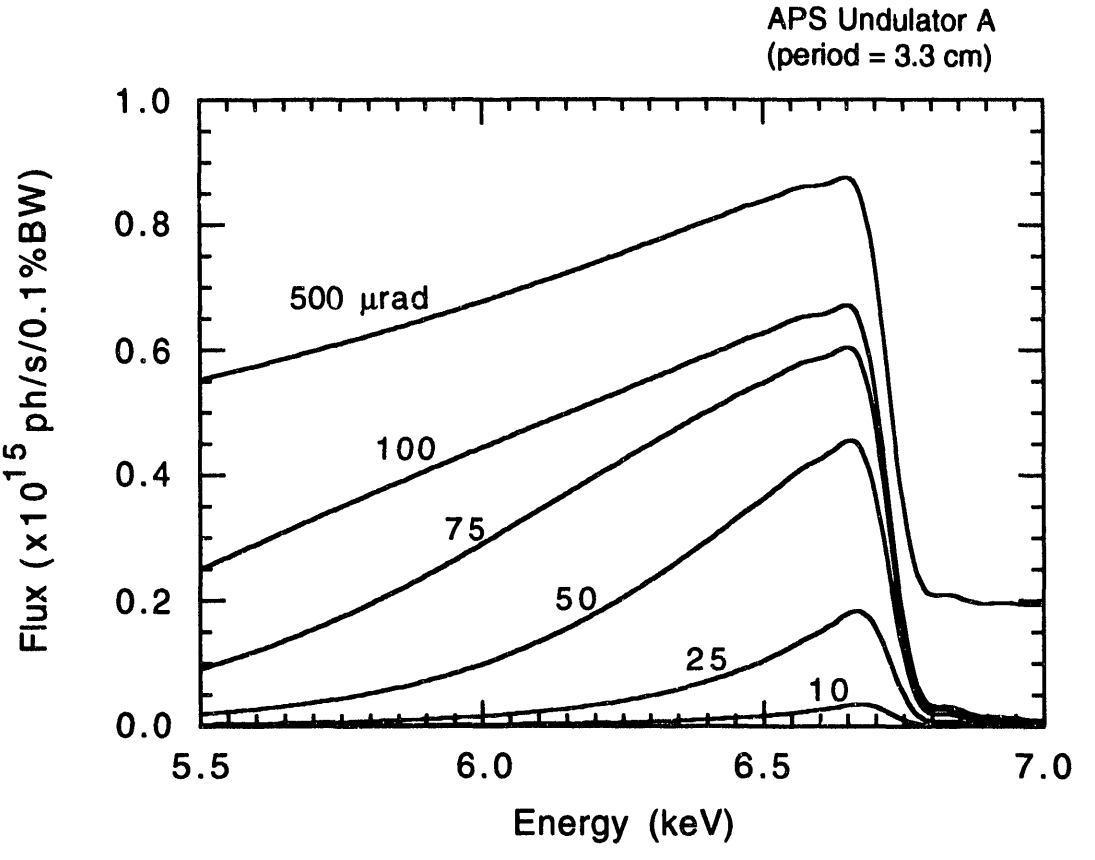

Fig. 16 Spectral flux of the first harmonic through square apertures of various sizes for the initial phase (K=1.48). (Operation at 7 GeV, 100 mA).

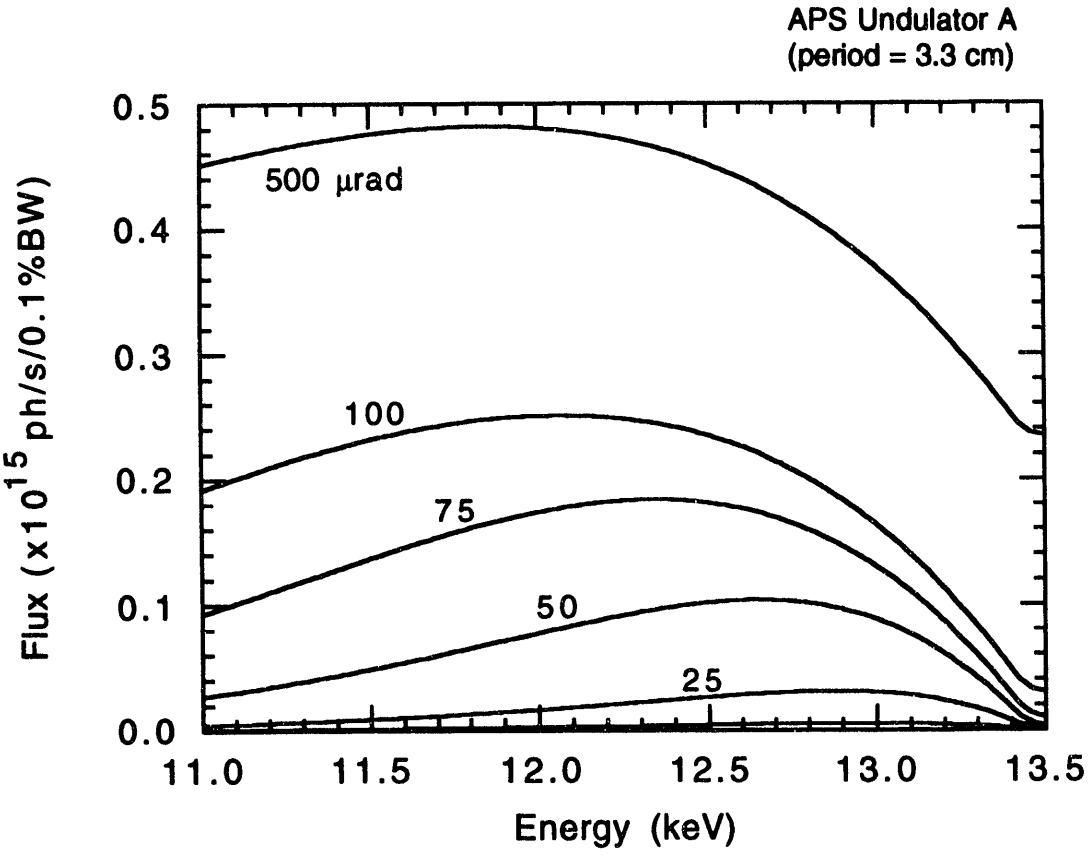

Fig. 17 Spectral flux of the second harmonic through square apertures of various sizes for the initial phase (K=1.48). (Operation at 7 GeV, 100 mA).

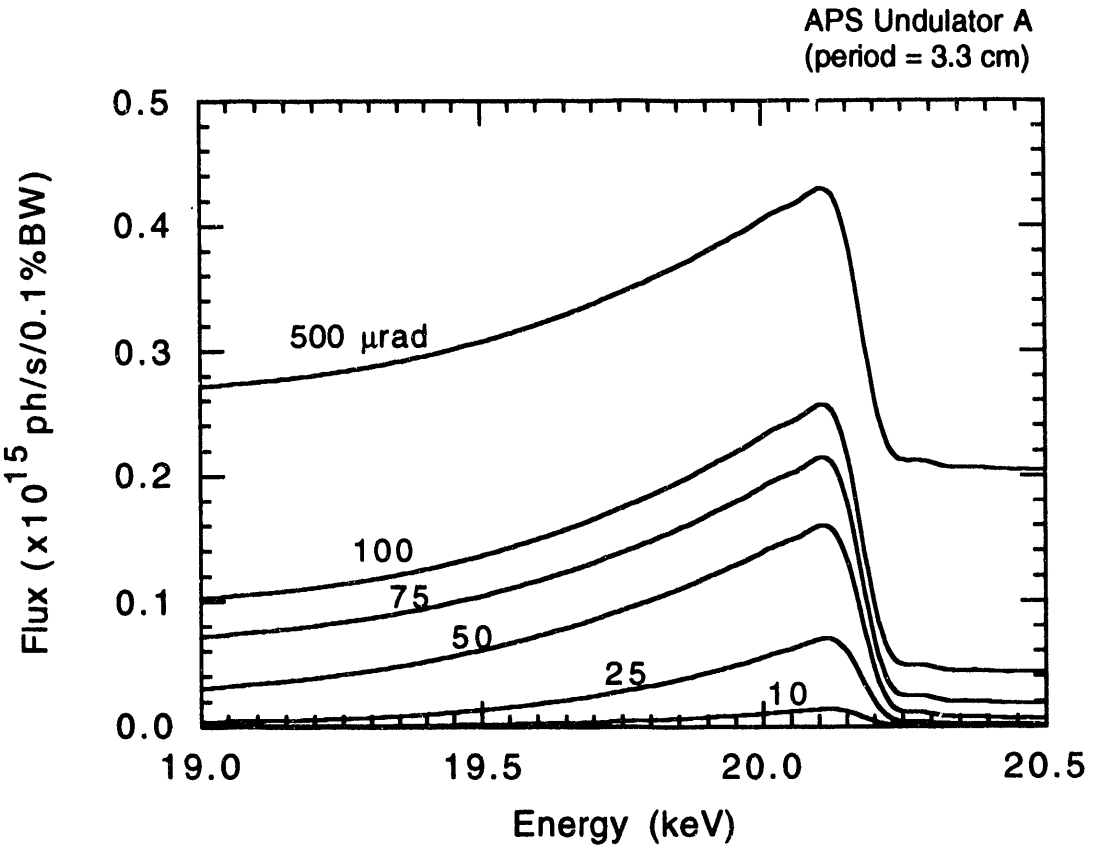

Fig. 18 Spectral flux of the third harmonic through square apertures of various sizes for the initial phase (K=1.48). (Operation at 7 GeV, 100 mA).

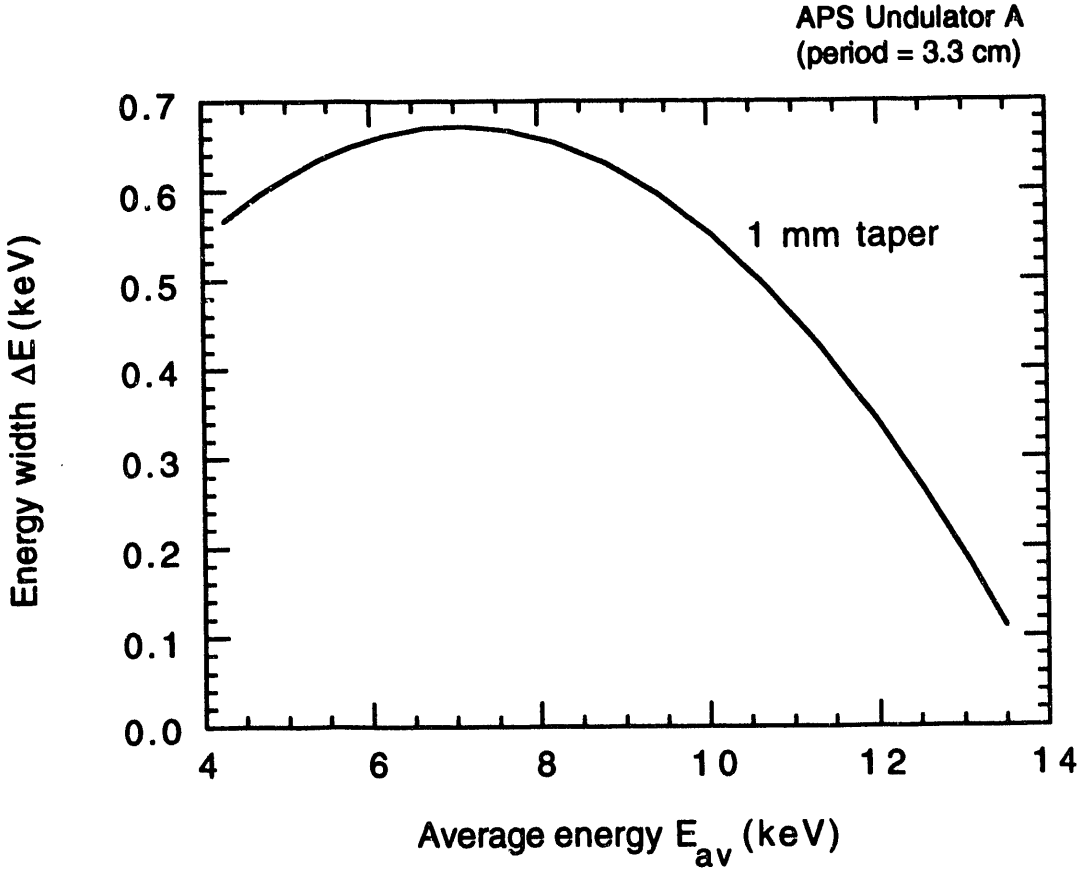

Fig. 19 Energy width ΔE due to 1-mm tapering as a function of the average energy of the first harmonic. Data are generated using Eq. 8. The ΔE plotted here can be scaled with the amount of tapering ΔG and the harmonic number n.

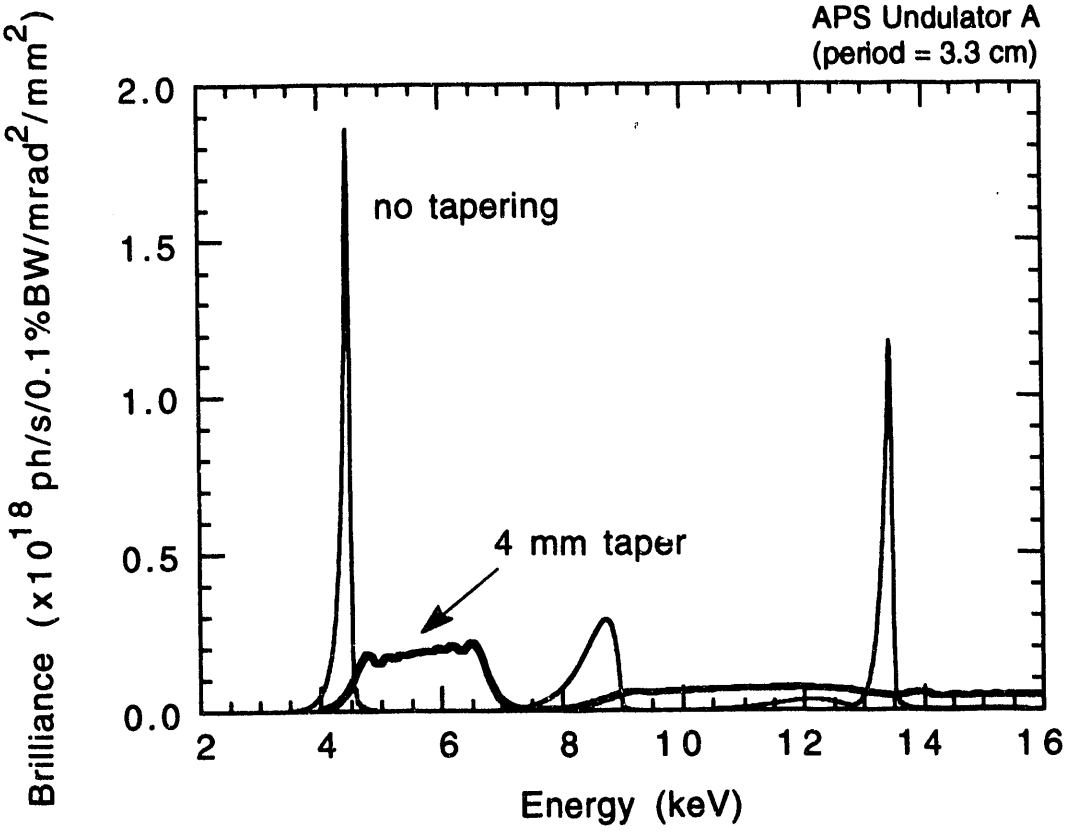

Fig. 20 On-axis brilliance spectrum for no tapering and 4-mm tapering at closed gap. One end of the undulator is fixed at a 1.2 cm-gap in both cases. (Operation at 7 GeV, 100 mA).

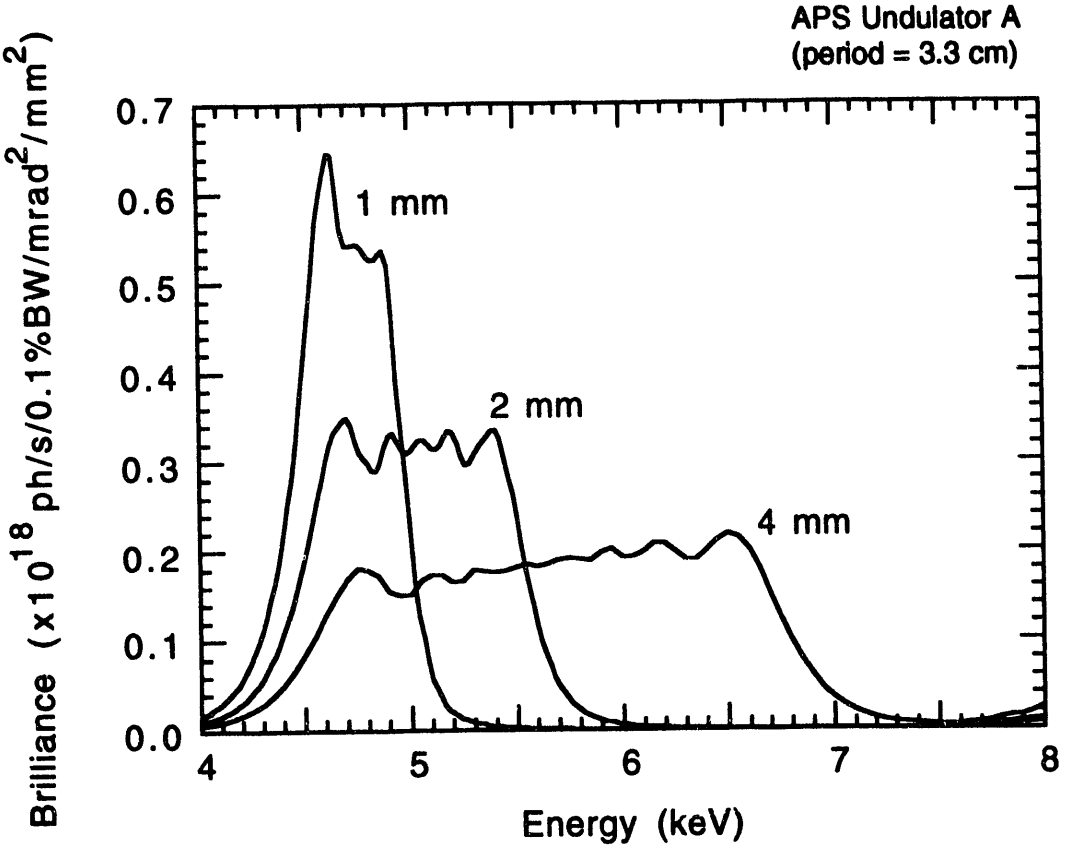

Fig. 21 On-axis brilliance spectrum of the first harmonic at 1, 2, and 4 mm tapering. One end of the undulator is always fixed at a gap of 1.2 cm, while the other end opens up. (Operation at 7 GeV, 100 mA).

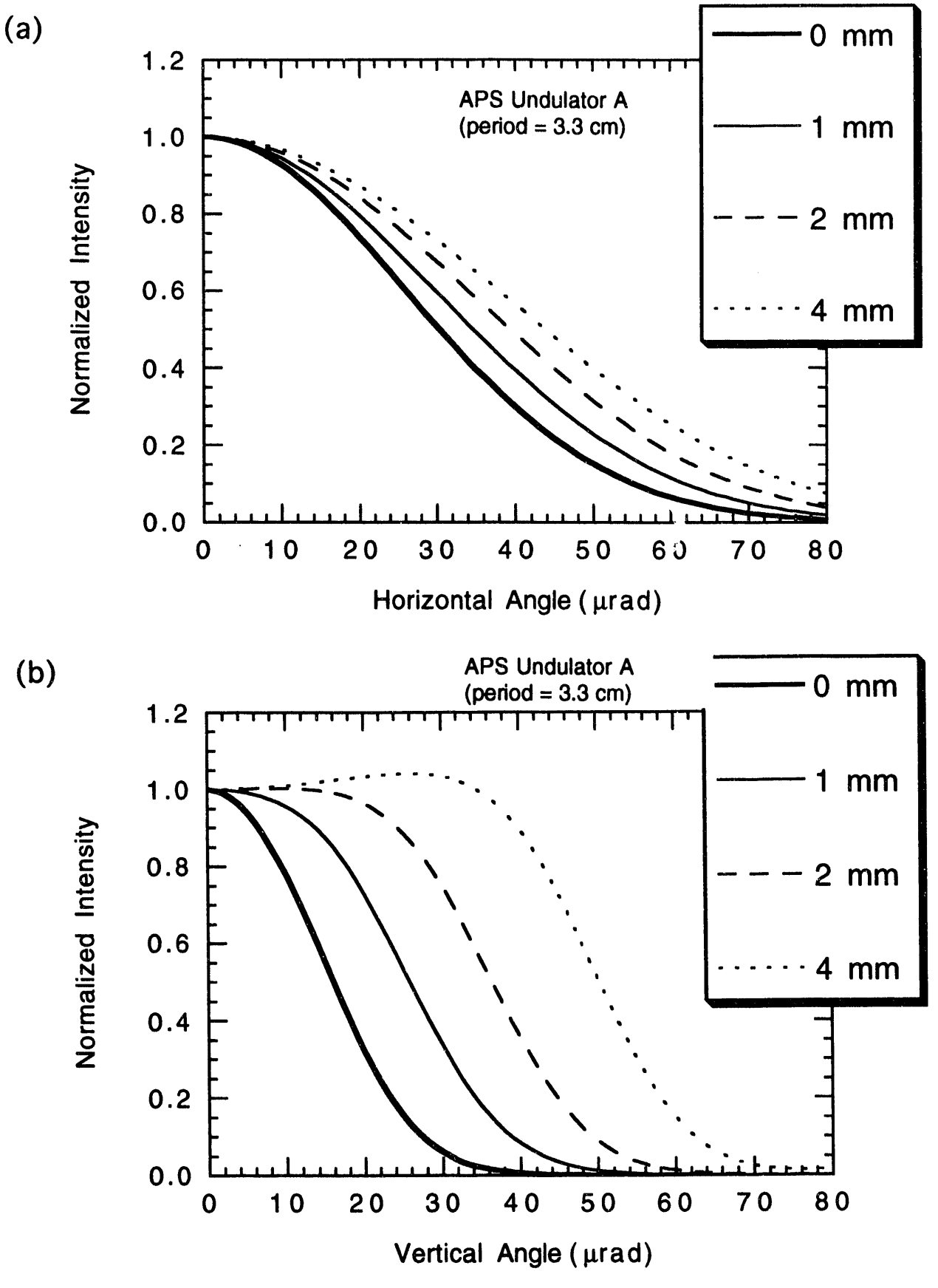

Fig. 22 Angular distribution along the horizontal and vertical directions at the respective average energy E_{av} for each of the three tapering cases (see Table 4). All the data have been normalized to 1 at θ=0.

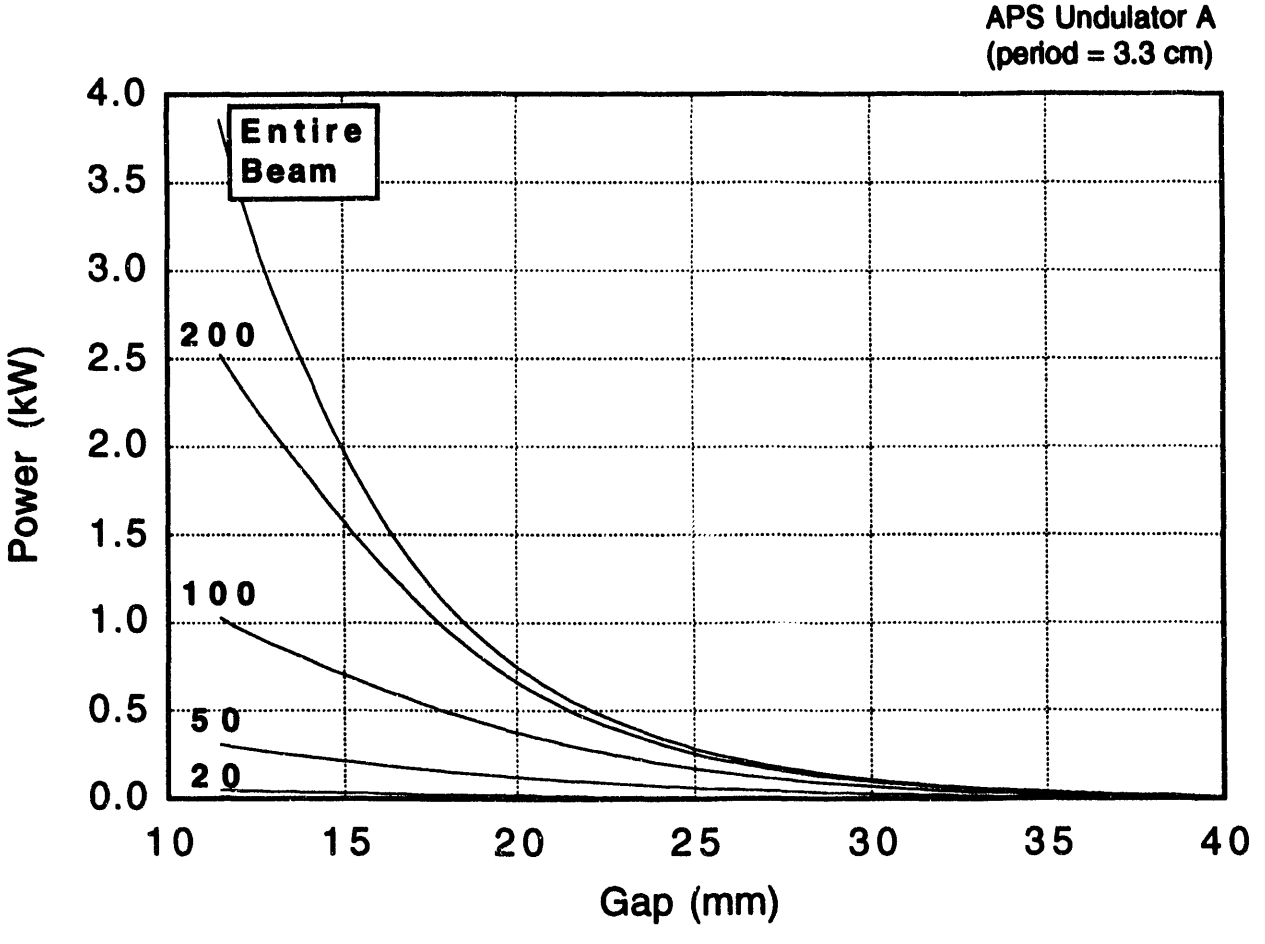

Fig. 23 Total power through square apertures of various sizes, as a function of the gap opening. The dimension of each side of the square (in μrad) is given (Operation at 7 GeV, 100 mA).

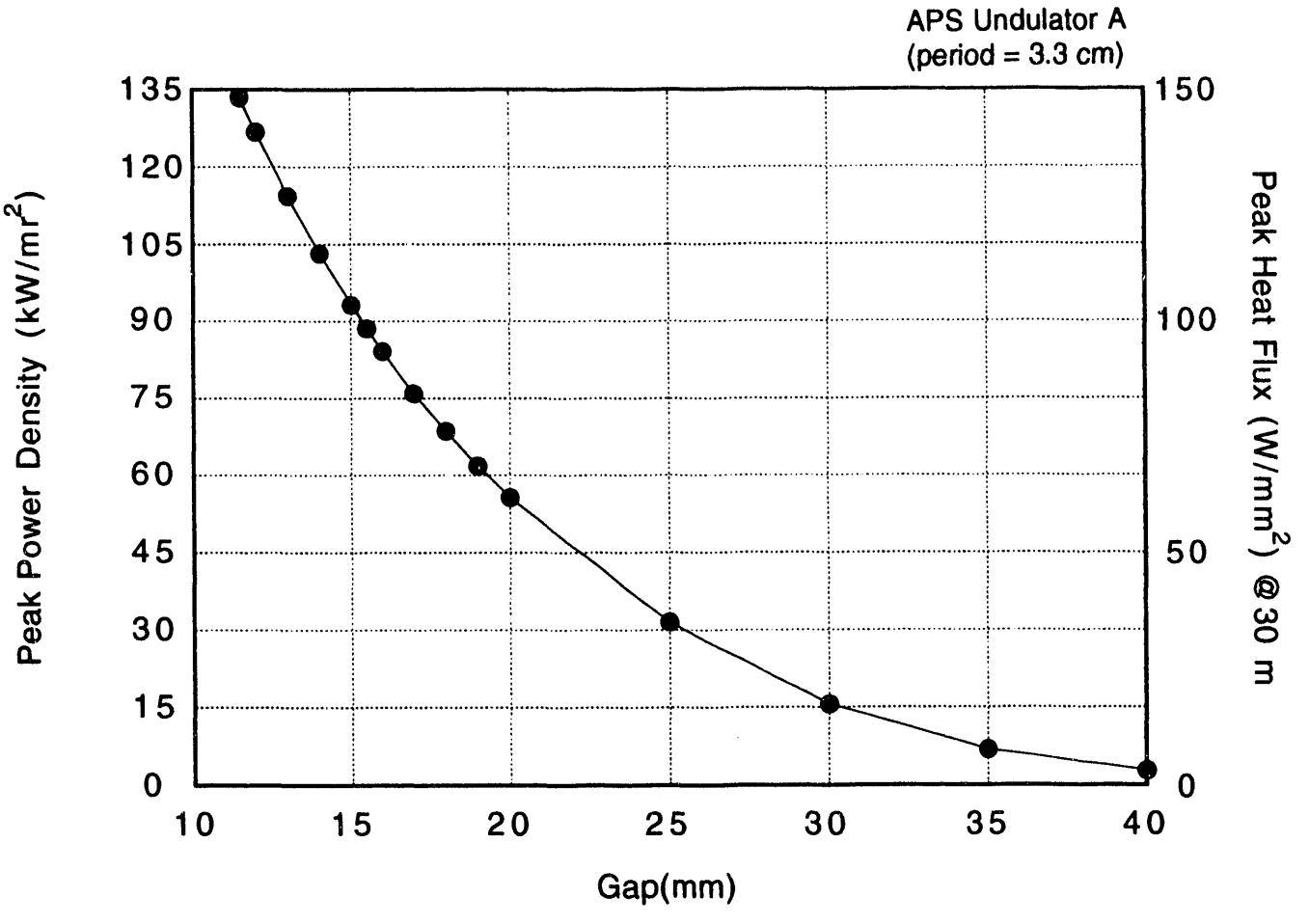

Fig. 24 Peak power density of Undulator A as a function of gap opening. The corresponding values for the peak heat flux normal to the beam at 30 m from the source can be read from the y-axis on the right. (Operation at 7 GeV, 100 mA).

END

DATE
FILMED
4/28/93